



HAL
open science

Closed-loop separation control over a sharp edge ramp using genetic programming

Antoine Debien, Kai A. F. F. von Krbek, Nicolas Mazellier, Thomas Duriez,
Laurent Cordier, Bernd R. Noack, Markus W. Abel, Azeddine Kourta

► **To cite this version:**

Antoine Debien, Kai A. F. F. von Krbek, Nicolas Mazellier, Thomas Duriez, Laurent Cordier, et al..
Closed-loop separation control over a sharp edge ramp using genetic programming. *Experiments in
Fluids*, 2016, 57 (40), pp.40. 10.1007/s00348-016-2126-8 . hal-01358992

HAL Id: hal-01358992

<https://hal.science/hal-01358992v1>

Submitted on 16 Nov 2024

HAL is a multi-disciplinary open access archive for the deposit and dissemination of scientific research documents, whether they are published or not. The documents may come from teaching and research institutions in France or abroad, or from public or private research centers.

L'archive ouverte pluridisciplinaire **HAL**, est destinée au dépôt et à la diffusion de documents scientifiques de niveau recherche, publiés ou non, émanant des établissements d'enseignement et de recherche français ou étrangers, des laboratoires publics ou privés.

Closed-loop separation control over a sharp edge ramp using Genetic Programming

Antoine Debien^{*1}, Kai A. F. F. von Krbek^{†2}, Nicolas Mazellier¹, Thomas Duriez⁵, Laurent Cordier², Bernd R. Noack^{2,3}, Markus W. Abel⁴, and Azeddine Kourta¹

¹Université d'Orléans, INSA-CVL, PRISME EA 4229, 8 rue Léonard de Vinci, F45072, Orléans, France

²Institute PPRIME, CNRS – Université de Poitiers – ENSMA, UPR 3346, Département Fluides, Thermique, Combustion, CEAT, 43 rue de l'Aérodrome, F-86036 Poitiers Cedex, France

³Also at: Institut für Strömungsmechanik, Technische Universität Braunschweig, Hermann-Blenk-Straße 37, D-38108 Braunschweig, Germany

⁴Ambrosys GmbH, Albert-Einstein-Straße, D-14473 Potsdam, Germany

⁵CONICET, Universidad de Buenos Aires, Ciudad Autonoma de Buenos Aires, Argentina. Formerly at: Institute PPRIME, Poitiers, France

July 30, 2018

Abstract

We experimentally perform open and closed-loop control of a separating turbulent boundary layer downstream from a sharp edge ramp. The turbulent boundary layer just above the separation point has a Reynolds number $Re_\theta \approx 3500$ based on momentum thickness. The goal of the control is to mitigate separation and early re-attachment. The forcing employs a spanwise array of active vortex generators. The flow state is monitored with skin-friction sensors downstream of the actuators. The feedback control law is obtained using model-free genetic programming control (GPC) (Gautier et al. 2015). The resulting flow is assessed using the momentum coefficient, pressure distribution and skin friction over the ramp and stereo PIV. The PIV yields vector field statistics,

e.g. shear layer growth, the back-flow area and vortex region. GPC is benchmarked against the best periodic forcing. While open-loop control achieves separation reduction by locking-on the shedding mode, GPC gives rise to similar benefits by accelerating the shear layer growth. Moreover, GPC uses less actuation energy.

1 Introduction

Fluid flows have an important impact on the performance of ground or airborne transport vehicles, of gas and oil pipelines and of chemical and pharmaceutical processes, just to name a few applications. Hence, the optimization of such flows by passive or active means to increase engineering performance constitutes a very core discipline of fluid mechanics (Brunton and Noack, 2015). Passive flow control can provide an increase of performance without energy con-

^{*}antoine.debien@onera.fr

[†]Kai.von.Krbek@krbek.de

sumption. For instance, vortex generators on the wings of most passenger aircrafts prevent early separation and thus increase lift and reduce drag. The effect of many passive devices can be emulated by active ones, e.g. fluidic jets may act as active vortex generators. Such active control can be turned on just in case of need, or turned off to prevent parasitic drag. Active flow control is a key for further improvement for transport vehicles and combustion (King, 2007, 2010). In particular, feedback control can bring distinct benefits over blind open-loop forcing (Rowley and Williams, 2006), e.g. can counteract instabilities in-time, perform disturbance rejection and compensate for model uncertainty.

The focus of this study is separation mitigation. Separation occurs in many flow processes and may imply detrimental effects such as lift reduction, drag increase and noise generation. Downstream of the separation point, a shear layer develops and transports vorticity far from the wall. Large scale spanwise vortices emerge from the roll-up of the shear layer vorticity induced by the Kelvin-Helmholtz instability (Mittal et al, 2005; Tennekes and Lumley, 1972). The Kelvin-Helmholtz instability is characterized by the Strouhal number $St_\theta = 0.012$ based on the boundary layer momentum thickness θ close to the mean separation point (Hasan, 1992; Zaman and Hussain, 1981). As the shear layer emerges from the separation point, spanwise vortices progressively grow and merge. This process leads to the shedding mode, characterized by a Strouhal number $St_{L_{sep}} = 0.6-0.8$ (Cherry et al, 1984; Dandois et al, 2007; Mabey, 1972) based on the separation length L_{sep} and the free velocity flow field U_∞ .

Vortex generators (VGs) are a passive flow control device which may efficiently delay separation (Lin, 2002; Godard and Stanislas, 2006a). VGs induce an array of streamwise vortices energizing the near wall flow by momentum transfer with the free-stream. However, these VGs are permanently fixed to the system and come with a parasitic drag even in operating conditions where they are not needed. Thus, these can induce drag penalties (Lin, 2002) if flow control is just needed during specific phases.

By contrast, active flow control, which adds energy in the flow using actuators, can be switched-off

when control is not needed. Active separation control strategies are usually relying on optimal reduced frequencies F^+ to delay or shift a separation. In this paper, F^+ is scaled with L_{sep} and U_∞ . According to literature, the optimal frequency range presents a large variability. For example, Seifert and Pack (2003) emphasized the efficiency of $0.5 \leq F^+ \leq 1.5$ while Greenblatt and Wygnanski (2000) highlight an optimal reduced frequency range $2 \leq F^+ \leq 4$ and Amitay and Glezer (2002) show the possibility to use $F^+ \geq 10$.

This large frequency range suggests to adapt the control by closing the loop with sensors. Adaptive control approaches like extremum or slope seeking have shown good results for optimization (Benard et al, 2010; Shaqarin et al, 2013). However, an effective in-time control of large-scale coherent structures or dominant instabilities needs to respect the flow physics for the control design. This design may be model-based using reduced-order models (Gerhard et al, 2003; Pastoor et al, 2008) to account for nonlinear actuation dynamics. Evidently, the control law depends on the quality of the flow model. Such a model is still a challenge (Cordier et al, 2013) for broad-band turbulence dynamics with frequency cross-talk preventing a meaningful local linearization.

On the other hand, a model-free control design using powerful methods of Machine Learning (Murphy, 2012) has been shown to be highly effective in a number of experiments (Duriez et al, 2014; Gautier et al, 2015; Parezanovic et al, 2015). This approach, called *Genetic Programming Control* (GPC) in the sequel, detects and exploits nonlinear actuation mechanisms in an unsupervised manner. GPC has outperformed the best open-loop control in terms of robustness and has worked even in case of a demonstrated nonlinear relation between actuators and sensors. The key enabler is the application of genetic programming, a classical method of symbolic regression (Koza, 1992), to optimize the closed-loop control law. As such, GPC can be viewed as a generalization of the genetic algorithms often used to identify the parameters of control laws. We refer to the review article of Brunton and Noack (2015) for an in-depth discussion of model-based and model-free turbulence control strategies.

In this paper, closed-loop control separation is performed using GPC and benchmarked with an optimized open-loop control where vortex shedding is locked-on, leading to a reduction of the separation bubble (Debien et al, 2015). The control is introduced by Active Vortex Generators (AVGs) which are set-up similarly to the optimal configuration determined by Godard and Stanislas (2006b) and Cuvier et al (2011).

The experimental setup including the description of the facility, the model, the actuators/sensors and measurement chains is detailed in Sec. 2. The GPC algorithm used for the control design is then described in Sec. 3 with a special attention paid to the experimental implementation. In particular, we define the cost functional used to rank the different GPC individuals as a compromise between the reduction of the separation length and the value of the momentum coefficient needed to achieve it. In Sec. 4.1, results of the best open and closed-loop experiments are presented based on the measurements made during the GPC runs. At this stage, eight particular GPC individuals performing well during the learning process are highlighted and discussed. To understand the mechanisms behind the best performing control laws, these individuals are further analysed in Sec. 4.2 by including PIV measurements and by increasing the evaluation times used for characterizing the control laws. The performance of the different individuals is then evaluated in terms of the AVGs' characteristics, of the separation length and of the energetic impact on the flow. Finally, in Sec. 4.3, the properties of the mixing layer resulting from one of the most efficient GPC individuals are benchmarked with the best open-loop in terms of vorticity thickness, turbulent kinetic energy, Reynolds stresses and distribution of vortex region area.

2 Experimental Setup

2.1 Wind tunnel and test section

The experiments are performed in the "Lucien Malavard" subsonic wind tunnel located at the PRISME Laboratory, University of Orléans. The test

section is 2 m high, 2 m wide, and 5 m long. The maximum free-stream velocity in the test section is 60 m/s, and the residual turbulence intensity is below 0.4%. The ramp model (see Fig. 1) is set at the mid-height of the test section and spans the tunnel's width. The model is comprised of four parts: an elliptic leading edge, a flat plate that enables the development of a new, thin, boundary layer, a downward sloping ramp, and a second flat plate for the recovery region. Furthermore, a controllable flap is fixed at the trailing edge to control the stagnation point at the leading edge and to minimize the circulation around the model. This flap is set at an incidence of 7° to ensure a symmetrical pressure distribution at the leading edge. The ramp has a length of $l = 470$ mm and a step height of $h = 100$ mm. The edge ramp is located at $x/h = 0$ with a slant angle of 25° ending with a 7th order polynomial given by:

$$\frac{y}{h} = 1 - 35 \left(\frac{x}{l}\right)^4 + 84 \left(\frac{x}{l}\right)^5 - 70 \left(\frac{x}{l}\right)^6 + 20 \left(\frac{x}{l}\right)^7, \quad (1)$$

for $0.5 \leq x/l \leq 1$.

For all the results presented in this paper, the free-stream velocity is set to 20 m/s, achieving a Reynolds number $Re_\theta \approx 3500$ based on momentum thickness just above the sharp edge ramp. The boundary layer is tripped to fix the transition, thus warranting the reproducibility of its properties during the overall experiments. Further characterization of the unactuated flow (hereafter called baseline) is provided in Debien et al (2014).

2.2 Active vortex generators (AVG)

For introducing the control, 54 AVGs in counter-rotating configuration are employed. Each AVG is composed of two jets (Fig. 2), leading to the generation of two counter-rotating streamwise vortices that are triggered and driven in on/off mode. These AVGs are positioned using the set of optimal parameters determined by Godard and Stanislas (2006b) and Cuvier et al (2011). The AVGs are placed one boundary layer thickness upstream of the sharp edge ramp. The diameter of the exit holes is $\Phi = 1.2$ mm. The direction of the jets is characterized by the pitch and skew angles $\alpha = 135^\circ$ and $\beta = 45^\circ$, respectively.

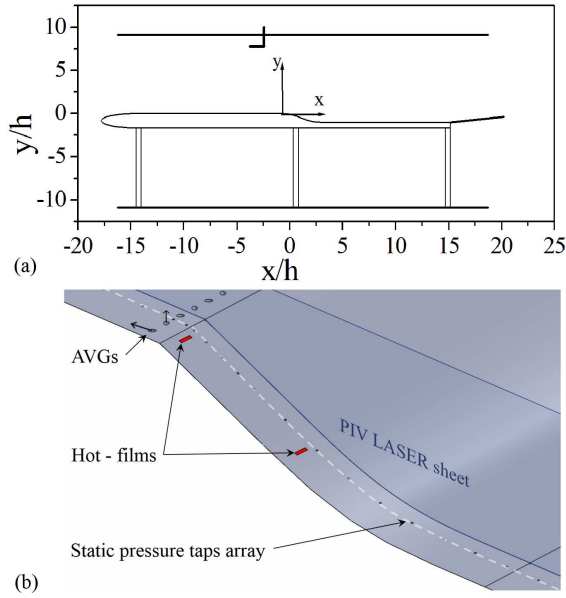


Figure 1: a) Wind tunnel setup and b) close-up of the sharp edge ramp with the measurement facilities(not true to scale).

The distance between two jets of the same actuator is $\lambda/\Phi = 15$, and the transverse distance between the center line of two consecutive AVGs is $L/\Phi = 30$. The jets' velocity ratio is regulated to be close to $V_{Jet}/U_\infty = 3$.

All the AVGs are supplied with air through a plenum chamber pressurized with compressed air coming from the Laboratory network. Due to the shape and size of the model, the plenum is divided into two sets of tanks. The first one of capacity 90 L is placed outside of the test section. In order to compensate for the pressure loss over the long tubing (4 m) connecting the tank to the actuators, a set of three tanks of smaller capacity (20 L each) is embedded in the profile, directly at the exit slots. Nine triggered electro-valves with sonic throats are connected to each of these three tanks. Each electro-valve supplies in on/off mode two pairwise AVGs, *i.e.* a total of 4 jets.

The exit velocity of the jets is estimated using a calibrated 4th order polynomial by measuring the pres-

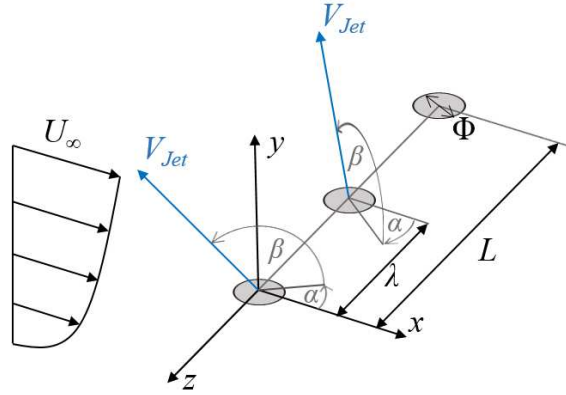


Figure 2: Active vortex generators (counter-rotating configuration).

sure inside the second set of tanks. The pressure is measured by a differential pressure sensor (5 bar, ± 100 Pa, 0.1% FSO) and is regulated by a mass flow controller (Brooks, 5853 E series) providing up to 500 L/min. A performance evaluation of this system showed that the pressure loss in the tank is less than 1.3% when AVGs are used in on/off mode with a constant actuation frequency f_{Pulse} in the range of $10 \text{ Hz} \leq f_{Pulse} \leq 100 \text{ Hz}$ (at 50% duty cycle), corresponding to a velocity jet variation of 3%.

Based on the determination of V_{Jet} , the momentum coefficient c_μ is estimated as

$$c_\mu = \frac{\rho_{Jet} S_{Jet} D_c V_{Jet}^2}{\frac{1}{2} \rho_\infty S_{Ref} U_\infty^2}, \quad (2)$$

where ρ_{Jet} is the flow density at the exit of the actuator, ρ_∞ is the free-stream density, D_c the duty cycle, S_{Jet} is the total cross section of the 108 blowing jets, and S_{Ref} the streamwise projected area of the ramp (height \times spanwise length).

2.3 Hot-film measurements

For evaluating the performance of a given closed-loop control law, GPC needs to measure local flow characteristics. In the experiments, the wall shear stress at the ramp surface is measured on two locations (see Fig. 1) using hot-film probes. These sensors give a

monotonic signal of the absolute shear stress value (Godard and Stanislas, 2006b; Cuvier et al, 2011; Shaqarin et al, 2011), which is directly induced by the local near wall velocity gradient. The two hot-films are located within the recirculation bubble of the separation for the baseline flow. Due to the actuation, the separation length decreases leading to an increase of the recirculation velocity within the recirculation bubble. This could lead to a non-monotonic variation of the hot-film signals with respect to the separation length. In particular, if the separation length is decreased, a change in the hot-film signal leads to an ambiguous interpretation. Indeed, the recirculation velocity increases which leads to an increasing wall shear stress on the sensors. If one is able to decrease the separation length even further, the attachment point may be moved progressively towards the hot-film sensors yielding a significant reduction of the wall shear stress. Thus, an evaluation of the control effectiveness based solely on the hot-film sensor value is not sufficient. Therefore, a set of static pressure sensors located along the span are also used to assess the effectiveness of the control (see Fig. 1).

Senflex SF9902, made of active Nickel elements, are used as hot-film probes. These sensors are 1.5 mm long, 0.102 mm wide, and are deposited on a polyamide substrate with a thickness less than 0.2 mm. They are glued directly on the model's surface with 76 μm double-sided tape at $x/h = 0.06$ and $x/h = 1.38$ (Fig. 1). The conditioning of the signal is achieved using a Dantec 90H02 Flow Unit. The signal from the anemometer was low-pass filtered at 300 Hz and conditioned on a 0 – 3.3 V range before feeding the signal into an Arduino. In section 3, this Arduino will be tasked to calculate in real-time the actuation based on the data of the hot-film sensors.

2.4 Pressure measurements

The pressure distribution along the ramp model is obtained using a PSI 8400 acquisition unit (2500 Pa, ± 0.75 Pa) which allows the measurement of the 80 pressure transducers inserted into the model. The pressure taps (0.3 mm in diameter) are connected to pressure sensors by a 1.5 m long tygon capillary. Time-series of fluctuations pressure are acquired with

a 200 Hz sampling frequency. During the GPC process, the pressure distribution over the ramp ($0 \leq x/h \leq 4.5$) is measured using a recording time of $1000 U_\infty/h$, corresponding to an uncertainty in the estimation of the pressure coefficient ($C_p = \frac{P-P_\infty}{1/2\rho_\infty U_\infty^2}$) of $\pm 7.5\%$. The pressure distribution for the baseline, the open-loop case and the best GPC individuals is then obtained using a recording time of $90000 U_\infty/h$. This allows to determine the pressure coefficient with an uncertainty estimation of $\pm 1\%$.

2.5 Particle image velocimetry and vortex detection

Finally, for evaluating and analyzing the baseline, the best open-loop actuation, and the best closed-loop actuation laws (see section 4), the vector field statistics are obtained with a Stereoscopic PIV acquisition system (LaVision) and its DaVis 7.3 software. Three-component PIV measurements are taken in the vertical symmetry plane of the downward flow induced at the mid-plane of one AVG (see Fig. 1). An Nd:YAG laser (Quantel, EverGreen) generating two pulses of 200 mJ each at a wavelength of 532 nm is located above the test section. A streamwise slit in the test section roof enables the vertical laser light sheet to reach the model. Images are captured with two CCD cameras (Imager LX 11M) mounted on opposite sides of the light sheet to obtain forward-scattering. Finally, Scheimpflug adapters are used to obtain a focused area despite the viewing angle of about 45° . The vector fields are computed with a final interrogation window of 32×32 pixels (50% overlap), giving a grid of 256 points in the streamwise direction and 148 points in the transverse direction. The space resolution is 2.4 mm corresponding to $0.024 x/h$. The vector field statistics are achieved with the capture of 2500 independent vector fields acquired at a sampling frequency of 1.6 Hz. This leads to statistical errors of the mean and second-order moments equal to 1% and 3%, respectively, for a 97% confidence interval (Benedict and Gould, 1996).

Instantaneous PIV vector fields are also used to characterize two-dimensional vortex regions. Many classical algorithms of vortex extraction (λ_2 and

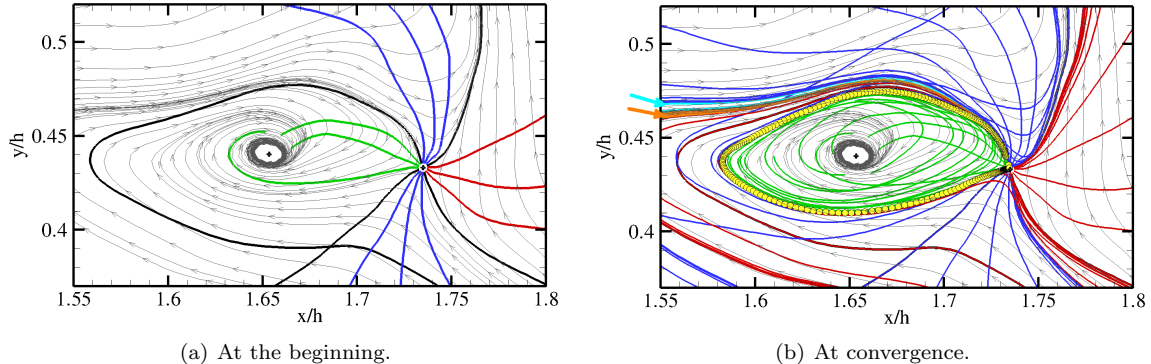


Figure 3: Concept of closed lines γ_ϕ starting from a saddle point. (a) illustrates the situation at the beginning of the algorithm, whereas (b) corresponds to the solution at convergence. Streamlines of the vector field are depicted in light gray. Black solid lines correspond to the lines starting in the principal directions of the saddle point. Colour lines refer to the boundary condition of each line (blue: exit of velocity field ; green, red, cyan and orange: attraction by a critical point). The cyan and orange arrows in (b) highlight two vortex region candidates created by the extraction algorithm. The area materialized by yellow circles corresponds to the vortex region Ω associated to the closed lines drawn in green.

Okubo-Weiss Q criteria for instance) are based on a scalar indicator function, whose magnitude relates to the strength of vortex activity. In this framework, the extracted regions depend on a threshold value that is often chosen arbitrarily. Furthermore, methods based on this approach often do not identify correctly individual vortices and are usually not able to separate adjacent vortices. Another approach for determining the shape of a vortex is to purely rely on geometrical methods. Recently, Petz et al (2009) proposed an algorithm for vortex region extraction that makes use of vector field topology. Their definition of a vortex region is based on the generalization of the concept of closed streamlines loops. For a divergence-free vector field, the union of all closed streamlines defines intuitively a vortex region. By extension, the authors generalize the streamline criterion to vector fields with divergence, by introducing closed lines whose tangent present a constant incident angle to the vector field. The union of these lines defines a vortex region candidate that is discriminated by imposing that vortex regions are bounded by closed loops that start and end at saddle points.

It can be proved by continuity that at least one saddle point is included in the closure of a vortex region (Petz et al, 2009).

Figure 3 illustrates the concept of closed lines, hereafter denoted γ_ϕ , that intersect the flow field at a constant angle ϕ and enclose at least one saddle point. The tracing of the closed lines starts from a saddle point. The principal directions of the fixed point lead to the discrimination of four distinct regions for the closed lines, two oriented towards the upper and lower boundaries of the flow field, and two oriented toward upstream and downstream vortices. As an illustration, let Ω be the region oriented toward the core vortex in Fig. 3. Mathematically, this region is defined as $\Omega = \{\gamma_\phi \mid \phi \in [\phi_{\text{Min}}; \phi_{\text{Max}}]\}$ where ϕ_{Min} and ϕ_{Max} correspond to the angles specified by the two principal components designing the region. The lines γ_ϕ whose angle is close to the mean value of $[\phi_{\text{Min}}; \phi_{\text{Max}}]$ describe a straight path from the saddle point to the vortex core, whereas lines associated to angles close to ϕ_{Min} and ϕ_{Max} describe curves looping around the vortex core before reaching it (see green lines in Fig. 3(a)).

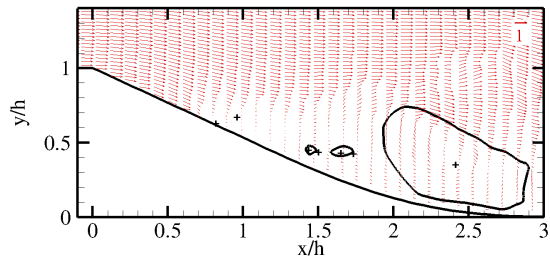


Figure 4: Instantaneous vector field velocity above the ramp and extracted vortex regions (black contours). The black crosses correspond to the detected critical points.

The algorithm of Petz et al (2009) presents two steps. First, the critical points from a vector field are extracted and sorted by class (saddle point, attracting/repelling node, attracting/repelling focus, center). The second step consists to trace the lines γ_ϕ for different values of ϕ and then to identify vortex region candidates by clustering neighbouring lines with similar behaviour. For each saddle point, the principal directions are determined and a first set of lines γ_ϕ is generated with a regular distribution of angles ϕ between two directions (see Fig. 3(a)). The type of boundary condition of each line (attraction to a critical point or exit of the velocity field) is then determined, allowing the creation of vortex region candidates by clustering the lines with the same boundary condition (see Fig. 3(b)). During the algorithm, new regions can be discovered and their bounds have also to be determined. This iterative process takes end when the boundary lines of two neighbouring regions present a difference of angle ϕ equal to $\pi/2^{15}$. The closed lines γ_ϕ and the critical points are kept during the algorithm. This allows to sort the different vortex regions (keeping one particular vortex region among the set of regions enclosing the same critical points) and to produce a hierarchy of vortex regions (several regions being enclosed in a larger one).

A typical example of the vortex regions extracted by this algorithm is presented in Fig. 4. This algorithm is used in Sec. 4.3 to determine the statistical distribution of the area of vortex regions for the different controlled flows.

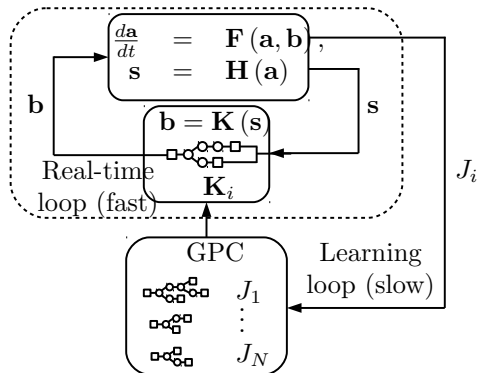


Figure 5: General principle of GPC. Two loops are present. The inner loop is the actual control loop which is on a real-time basis. The dynamical system (upper box) feeds the sensors \mathbf{s} to the controller (middle box). The controller uses the control law corresponding to the i -th individual (\mathbf{K}_i) in order to compute the actuation command \mathbf{b} which is fed back to the dynamical system. The outer loop is the evolutionary learning loop. The GPC algorithm (lower box) is providing the controller with control laws. After a statistically significant evaluation time, the cost function value J_i is computed for the control law \mathbf{K}_i . The GPC algorithm is using the individual values J_1, \dots, J_N to evolve the population of control laws until the control problem is solved.

3 Genetic Programming Control

3.1 Control Design

Genetic Programming Control (Parezanovic et al, 2015; Gautier et al, 2015) is a model-free control method designed to determine non-linear control laws for a non-linear complex dynamical system in an unsupervised, data driven manner. GPC is an evolutionary algorithm largely based on classical genetic programming (Koza, 1992; Koza et al, 1999) and adapted to determine experimental control laws.

A general view of the algorithm implementation can be seen in Fig. 5. The experiment is represented

by the dynamical system:

$$\begin{aligned} \frac{d\mathbf{a}}{dt} &= \mathbf{F}(\mathbf{a}, \mathbf{b}), \\ \mathbf{s} &= \mathbf{H}(\mathbf{a}), \\ \mathbf{b} &= \mathbf{K}(\mathbf{s}) \end{aligned} \quad (3)$$

with $\mathbf{a} \in \mathbb{R}^{N_a}$ representing the states, $\mathbf{s} \in \mathbb{R}^{N_s}$ representing the measurements on the system and $\mathbf{b} \in \mathbb{R}^{N_b}$ representing the control laws. \mathbf{F} , \mathbf{H} , \mathbf{K} are respectively the evolution operator, the measurement function and the control laws. The control problem is defined by a cost function $J(\mathbf{s}, \mathbf{b})$ to be minimized. In the GPC framework, the control laws are represented by expression trees, containing arbitrarily complex combinations of user defined functions, operations, sensors and random constants. The learning GPC process is used to determine the control law best fitted to be used in the inner real-time feedback loop. Once the best control law is determined, the learning loop can be disconnected.

The learning process is achieved as follows. A first population of N individuals representing the control laws \mathbf{K}_i with $i \in [1, \dots, N]$ is randomly created. Each of these individuals is tested in the real-time dynamical system loop during the evaluation time T . At the end of the evaluation time, a cost function value J_i is given to each individual \mathbf{K}_i . A selection process determines which individuals are chosen for the population evolution. For each of the N new individuals to produce, a tournament is achieved between randomly chosen evaluated individuals, the individual with the lowest cost function value being selected for evolution. The selected individuals then go through genetic operations: replication (copy of the selected individual to the next generation), mutation (partial random alteration of the content of the individual) and crossover (partial exchange of the content of two selected individuals). Also, the five best individuals of the evaluated population are directly copied into the next generation in order to ensure that the following generation is at least as good as the preceding one. These operations are illustrated in Fig. 6.

Additionally to this classical genetic programming implementation, GPC encompasses modifications to

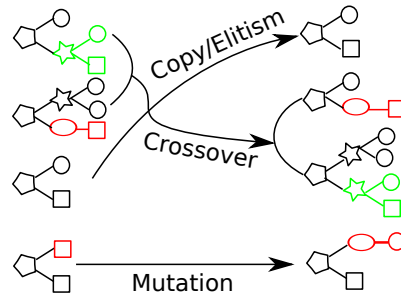


Figure 6: Graphical illustration of the different genetic operations: copy, crossover, mutation.

account for the experimental evaluation of the individuals: when an individual appears again in a new generation, it is further evaluated and its cost function value is averaged. Also, the three best individuals of each generation is reevaluated three times. This ensures that the convergence process is not dramatically affected by measurement noise and errors by eliminating intrinsically bad individuals that were accidentally assigned a low cost function value. Also it increases the statistical significance of the best individual's cost function value which allows to reduce the impact of having a suboptimal evaluation time T and then reduce the overall process time cost.

Once a new generation is created, a new evaluation of the whole population can be achieved. The learning process is stopped either when the cost function value of the best individual reaches a known global minimum (theoretical optimality stop criteria, though this is unlikely in an experiment), when no improvement has been achieved through several generations (empirical optimality stop criteria), when the minimal cost function value reaches a user predetermined value that reflects an acceptable performance (performance stop criteria) or when a prescribed number of generations has been reached (operational cost stop criteria). In those cases the best individual is used in the real-time controller and the learning loop can be disconnected.

3.2 Experimental Implementation

In the experiments, the GPC learning loop is implemented on a standard computer in Matlab, whereas the inner loop is implemented on an Arduino microcontroller. This Arduino acquires the experimental sensors signal and computes the control command sent to the actuators according to the current individual in the real-time closed-loop control. For each generation, the outer loop generates expressions for the individuals, compiles and uploads them on the inner-loop Arduino. The Arduino then loops between the evaluation of each control law \mathbf{K}_i during a time $T = 5$ s, with a 3 s resting time in between, and returns the cost function values J_i to the learning loop.

The mean values of the hot-film sensors for the baseline flow ($\text{HF}_{i,0}$) and for continuous blowing of the jets ($\text{HF}_{i,\text{Blow}}$) are used at the beginning of each generation and every 100 evaluations of the cost functions to normalize the hot-film sensors.

For each of the two hot-film sensors, three virtual sensors are created which leads in total to $N_s = 6$.

The first virtual sensor is calibrated to the average blowing and not blowing values, *i.e.*

$$s_i = \frac{\langle \text{HF}_i \rangle - \text{HF}_{i,0}}{\text{HF}_{i,\text{Blow}} - \text{HF}_{i,0}}, \quad i \in \{0, 1\}, \quad (4)$$

where $\langle \cdot \rangle$ denotes a moving average over ten measurements.

The second one is the instantaneous calibrated value of the sensor:

$$s_{i+2} = \frac{\text{HF}_i - \text{HF}_{i,0}}{\text{HF}_{i,\text{Blow}} - \text{HF}_{i,0}}, \quad i \in \{0, 1\}. \quad (5)$$

The calibration ensures that the virtual sensor values are close to the $[0, 1]$ interval. The third sensor is an instantaneous fluctuation calculated as:

$$s_{i+4} = s_{i+2} - s_i = \frac{\text{HF}_i - \langle \text{HF}_i \rangle}{\text{HF}_{i,\text{Blow}} - \text{HF}_{i,0}} \quad i \in \{0, 1\}. \quad (6)$$

The operators used to create the individuals are $+$, $-$, \times , $/$, \sin , \cos , \ln , \exp and \tanh . Sensitive operations such as $/$ and \ln are protected so that any value

in \mathbb{R} can be used as arguments. The absolute value of the denominator of $/$ is saturated to 10^{-2} . Also, $x \mapsto \ln(x)$ is modified to $x \mapsto \ln(|x|)$ for $|x| > 10^{-2}$ and $x \mapsto \ln(10^{-2})$ otherwise. Finally, the output of the constructed control laws is passed through the Heavyside function to transform the continuous output from \mathbf{K}_i to an on/off signal. If $b > 0$ (respectively $b < 0$), the control is on (respectively off).

The physical objective of the control problem is to re-attach the boundary layer in an energy efficient manner. The state of the boundary layer is assessed by the mean wall-friction measured by the hot-films and the average pressure distribution measured by the pressure taps. The actuation cost is assessed by the calculation of the average c_μ obtained from the flow meter on the pressure tank. This problem corresponding to a multi-objective optimization, the cost function used for GPC is defined as:

$$J = J_{\text{HF}} + \ell_{\text{PStat}} J_{\text{PStat}} + \ell_{\text{Act}} J_{\text{Act}} \quad (7)$$

where J_i , $i \in \{\text{HF}, \text{PStat}, \text{Act}\}$, corresponds to the cost functions for the different criteria to optimize and where ℓ_{PStat} and ℓ_{Act} are penalization coefficients.

The term J_{HF} related to the wall friction is calculated using:

$$J_{\text{HF}} = \frac{1}{N_{\text{HF}}} \sum_{i=1}^{N_{\text{HF}}} \left[1 - \tanh \left(\frac{\langle \text{HF}_i \rangle}{\text{HF}_{i,0}} - 1 \right) \right] \quad (8)$$

where N_{HF} is the number of hot-film sensors.

The term J_{PStat} related to the static pressure sensors is obtained using:

$$J_{\text{PStat}} = \int_T \frac{1}{0.1 + \sum_{i=1}^{N_{\text{P}}} (P(x_i) - P_0(x_i))^2 \frac{x_{\text{max}} - x_i}{x_{\text{max}} - x}|_{x=0}} dt, \quad (9)$$

where N_{P} is the number of static pressure sensors used for the estimation and x_i their streamwise coordinates. In the experiments, the estimation of J_{PStat} is based only on the pressure sensors located from the sharp edge ($x = 0$) to $x_{\text{max}} = 4.7h$. In addition, P_0 is the baseline pressure, and 0.1 in the denominator

is added to prevent the division by zero. The $J_{P_{Stat}}$ cost function penalizes an attachment point located far from the sharp edge and therefore large separation bubble as the separation point is fixed by the geometric discontinuity.

The actuation penalization term J_{Act} is obtained using:

$$J_{Act} = \int_T \frac{c_\mu}{V_{Jet}} dt. \quad (10)$$

In Sec. 4, we will keep constant the weight $\ell_{P_{Stat}}$ and analyse the influence of ℓ_{Act} on the best GPC actuation laws.

4 Results

The presentation of the results will be done in three steps. First, in Sec. 4.1, we present the GPC results through the data that are used during the Genetic Programming runs, *i.e.* the signal of the HF sensors, the pressure sensors, and the estimation of the momentum coefficient c_μ . Then, in Sec. 4.2, we perform an a posteriori analysis of the previous GPC results with the PIV measurements obtained offline. Finally, an in-depth analysis of a particular actuation law (individual 7), ranked among the most efficient by GPC, is done in Sec. 4.3. In the following, the use of individual and control or actuation law is strictly equivalent.

4.1 GPC Results

During the experimental determination of the closed-loop control laws, the use of the HF sensors is twofold: as an input signal for the computation of the control law, and to estimate J_{HF} according to (8). Both calculations are implemented in real time on the Arduino. The pressure data on the ramp is collected on a different computer and used to compute $J_{P_{Stat}}$ according to (9). These results are weighted with the estimation of J_{Act} to determine J needed to rank the individuals in the GPC algorithm.

Three different runs of genetic programming control are performed. For all the runs, the weight $\ell_{P_{Stat}} = \frac{1}{30}$ is kept constant. In addition, the probability of crossover, copy and mutation are fixed to

$p_{Cross} = 0.7$, $p_{Copy} = 0.1$ and $p_{Mut} = 0.2$, respectively. In order to test the influence of the amount of actuation on the results, three different values of penalization weights ℓ_{Act} are considered, namely 2.5, 0.8 and 0.6. $\ell_{Act} = 2.5$ corresponds to a strong penalization whereas setting $\ell_{Act} = 0.8$ and $\ell_{Act} = 0.6$ lower the level of penalization but still prevent constant blowing as a solution. Recently, Debien et al (2015)

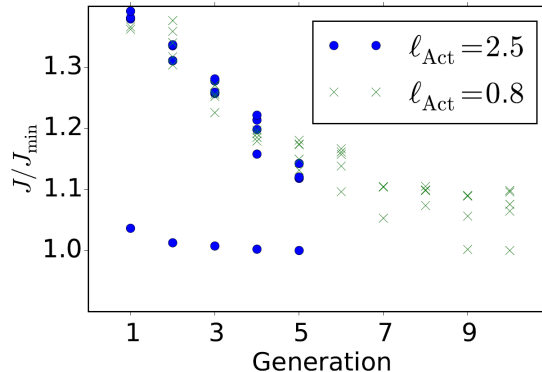


Figure 7: Variation of the normalized cost function value J over the generations for two GPC runs, one of 5 generations with $\ell_{Act} = 2.5$ and one of 10 generations with $\ell_{Act} = 0.8$. The five best individuals of each run are plotted. Even when the first generation contains already effective individuals (case $\ell_{Act} = 2.5$), we can note an overall improvement of the high ranking individuals of the population with 20 to 30% reduction of J in few generations. This demonstrates how the population is stirred towards the best individual to explore local minima and further improve the best result.

showed that for the same configuration of sharp edge ramp the best open-loop actuation has a frequency $f_{Pulse} = 30$ Hz and a duty cycle of 50%. In the following, we benchmark against this best periodic forcing eight particular actuation laws, namely: i) individuals 1 and 2 are taken out the first GPC run ($\ell_{Act} = 2.5$) after 5 generations, individual 1 being the best individual of all generations ; ii) individuals 3, 4, and 5 are the three best actuation laws obtained from the second GPC run ($\ell_{Act} = 0.8$) after 10 generations ; iii) individuals 6, 7, and 8 are obtained from

the third GPC run ($\ell_{\text{Act}} = 0.6$) after 5 generations, individual 6 being the best individual of all generations.

The evolution of the normalized cost function J over the generations is shown in Fig. 7 for two different values of ℓ_{Act} . For each generation, the J value of the five best performing actuation laws of each GPC run is plotted to show not only the improvement of the most effective control law but also to illustrate the global convergence of the population toward effective control laws for an increasing number of generations. One can see that with an increase of the number of generations, the performance of the best actuation would likely have increased. Due to experimental time constraints, the number of generations is kept low.

The J values for the different individuals are recorded in Tab. 1. These values are given, once with the specific value of ℓ_{Act} used during the GPC run, and once with an arbitrarily chosen value ($\ell_{\text{Act}} = 0.5$) to have a fair comparison with the best open-loop solution which has been chosen to achieve maximum performance regardless of actuation cost. The cost corresponding to each control problem defined by a different ℓ_{Act} value has also been computed for the best open-loop.

This table shows how GPC consistently finds closed-loop control laws performing better or similarly (where pure performance is predominant) to the best open-loop control as computed through the cost function used for their respective determination. Interestingly, at the exception of individual 2, all closed-loop control laws perform reasonably well with a cost function adjusted for low actuation cost ($\ell_{\text{Act}} = 0.5$). As a matter of fact, the $J|_{\ell_{\text{Act}}=0.5}$ values seem to indicate that all these individuals are roughly interchangeable. For instance individual 1 obtained with a high actuation penalization, individual 7 obtained with a low actuation penalization and the best open-loop show similar values. Nonetheless, the decomposition of the cost function in each of its constituent (see Tab. 2) shows that the final value of J is obtained through different mechanisms for each GPC determined individual: some focus on performance, others on economy.

This performance-actuation trade-off is further il-

Table 1: Performance comparison of the different actuation laws based on their J values. The penalization coefficients between the different terms of the J function were applied once with $\ell_{\text{Act}} = \ell_{\text{Act}}^{\text{Run}}$ kept at the value employed during the GP run and once with $\ell_{\text{Act}} = 0.5$ for comparison with the best open-loop control. The right column introduces the reference name of the GPC law in the manuscript. For details, see text.

	$J _{\ell_{\text{Act}}=\ell_{\text{Act}}^{\text{Run}}}$	$J _{\ell_{\text{Act}}=0.5}$	Reference
$\ell_{\text{Act}}^{\text{Run}} = 2.5$			
Best open-loop	1.14	0.38	
Best GPC law	0.88	0.38	Indiv. 1
Subopt. GPC law	1.12	1.00	Indiv. 2
$\ell_{\text{Act}}^{\text{Run}} = 0.8$			
Best open-loop	0.50	0.38	
Best GPC law	0.45	0.40	Indiv. 3
Subopt. GPC law	0.47	0.42	Indiv. 4
Subopt. GPC law	0.52	0.41	Indiv. 5
$\ell_{\text{Act}}^{\text{Run}} = 0.6$			
Best open-loop	0.42	0.38	
Best GPC law	0.42	0.39	Indiv. 6
Subopt. GPC law	0.45	0.41	Indiv. 7
Subopt. GPC law	0.46	0.45	Indiv. 8

Table 2: Performance comparison of the different actuation laws based on their J_i ($i \in \{\text{HF}, \text{P}_{\text{Stat}}, \text{Act}\}$) values. The weighting coefficients ℓ_i are not applied.

	J_{HF}	$J_{\text{P}_{\text{Stat}}}$	J_{Act}
Best open-loop	0.04	4.6	0.38
Indiv. 1	0.05	6.2	0.25
Indiv. 2	0.11	25.8	0.06
Indiv. 3	0.06	7.5	0.18
Indiv. 4	0.07	7.7	0.18
Indiv. 5	0.06	5.1	0.36
Indiv. 6	0.06	5.7	0.28
Indiv. 7	0.06	4.5	0.40
Indiv. 8	0.08	8.8	0.15

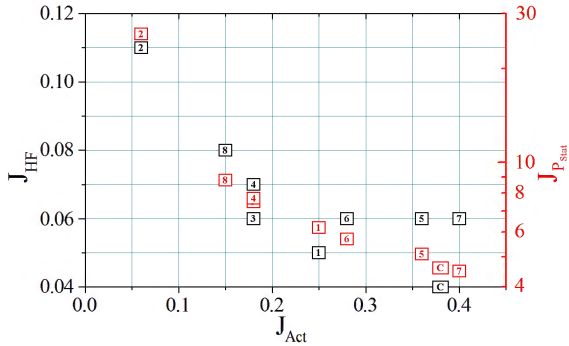


Figure 8: Variation of the cost function values J_{HF} and J_{PStat} versus J_{Act} for the GPC individuals and the best open-loop solution (label c).

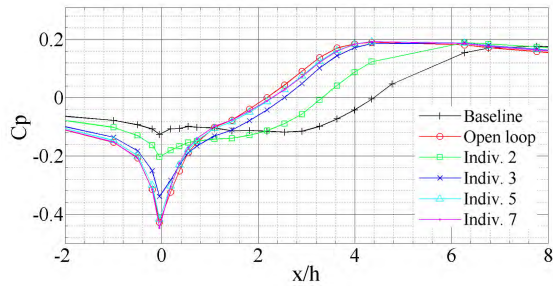


Figure 9: Pressure coefficient distribution over the ramp for the baseline, the best open-loop and some GPC individuals. Only the pressure sensors located in the range $0 \leq x/h \leq 4.70$ are used for estimating J_{PStat} .

illustrated in Fig. 8 where J_{HF} and J_{PStat} are plotted versus J_{Act} . We observe that J_{HF} and J_{PStat} vary as an hyperbolic function with respect to J_{Act} , even though a noticeable scatter can be seen for high values of the actuation penalty. This hyperbolic behaviour reflects the compromise between the cost of the control and its effectiveness. The set of solutions obtained by GPC is then equivalent to the Pareto frontier classically used in multi-disciplinary optimization. Due to the relatively large spacing of the pressure sensors, the determination of the position of the reattachment point using pressure sensors can not be inferred with accuracy and is therefore not

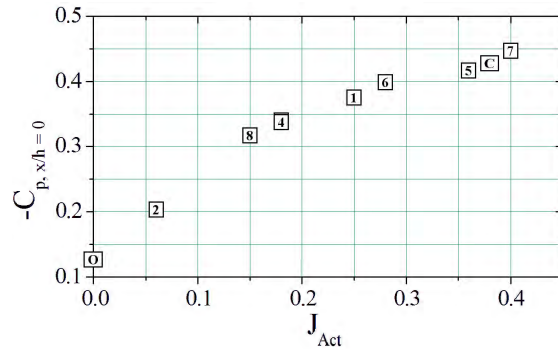


Figure 10: Pressure coefficient at the sharp edge ($x/h = 0$) versus J_{Act} for the baseline (label o), the best open-loop (label c) and the GPC individuals.

clearly visible in the J_{PStat} distribution. The evolution of the pressure coefficient (C_p) over the length of the ramp is presented in Fig. 9. Upstream of the sharp edge ($x/h = 0$), C_p gradually decreases towards the ramp due to a favourable pressure gradient induced by the proximity of the ramp and by the blowing of the AVGs. Downstream of the sharp edge of the ramp, the pressure rises up to its maximal value ($C_p \approx 0.2$) around the location of the reattachment point. Further downstream, the pressure converges towards $C_p \approx 0.19$. Figure 9 illustrates a direct relationship between actuation cost J_{Act} (as reported in Tab. 2) and separation control: the larger J_{Act} is, the smaller the separation length is. The C_p distribution measured for the GPC individuals approach to the one obtained for the best open-loop controller as J_{Act} increases. Whereas the pressure distribution around the attachment point provides a direct measurement of the effectiveness of the actuation, the pressure at the separation point (see Fig. 10) depends mainly on the momentum coefficient of the AVGs jets which generates a pressure minimum around the actuators.

Based on these criteria, four individuals seem to yield particular good results: individuals 1, 5, 6 and 7. Individual 5 and 7 present a J_{Act} value close to the best open-loop case whereas individuals 1 and 6 present a 34% and a 26% J_{Act} reduction, respectively, but also worse J_{PStat} values (see Fig. 8).

4.2 Analysis based on PIV measurements

Though the stereo PIV equipment is not able to feed its results in real-time in order to be used in the GPC process, it can be used to assess the controlled flow using the controllers obtained by GPC. In this section we provide an in-depth a posteriori analysis of the controlled flows obtained by GPC, with a detailed study of the actuation mechanism and evaluation from PIV of the flow features. A special focus is done on the individual 7 which appears to be the most interesting.

4.2.1 AVGs' characteristics

To evaluate the performance of the different control laws, the AVGs actuation characteristics are first examined. For the different control laws, the blowing velocity V_{Jet} of the AVGs and an estimated "duty cycle" are reported in Tab. 3. The blowing velocity is computed from a calibration law where the input is the pressure of the supplying tank. The "duty cycle" corresponds to the ratio between the AVGs' blowing duration and the total acquisition time. Using these values, the momentum coefficient c_μ and the energy flow rate of the blowing jets defined as

$$M_{Jet} = \rho_{Jet} S_{Jet} D_c V_{Jet}^3 \quad (11)$$

are computed.

Since blowing velocity is kept constant throughout experiments, the cost function J_{Act} mostly depends on D_c . However, it is worth noting that V_{Jet} may vary within a 5-7% range around its designed operating value. This occurs in high actuation frequency range ($f_{Pulse} \geq 250$ Hz) due to the limited time response of the valves. For the closed-loop cases, D_c is in the range between 0.07 and 0.49.

To get a better understanding about the control laws synthesized by the GPC, the statistical distribution of the actuation frequency is analysed. For that purpose, the instantaneous actuation frequency is inferred via a zero-crossing algorithm. The actuation signal being updated at approximately 1 kHz on the Arduino the discretization of the frequencies is larger at frequencies $f_{Pulse} \geq 100$ Hz.

Table 3: Characteristics of AVGs during the control phase.

	V_{Jet}	D_c	$c_\mu \times 10^{-4}$	M_{Jet}
Best open-loop	62.3	0.50	16.5	18.0
Indiv. 1	62.6	0.25	8.4	9.3
Indiv. 2	58.1	0.07	2.0	2.05
Indiv. 3	56.5	0.18	5.0	4.9
Indiv. 4	56.5	0.19	5.1	5.1
Indiv. 5	58.3	0.46	13.3	13.6
Indiv. 6	55.4	0.27	7.0	6.8
Indiv. 7	57.3	0.49	13.7	13.7
Indiv. 8	56.7	0.18	4.8	4.8

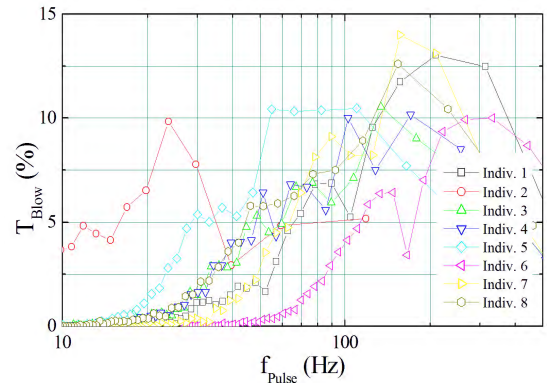


Figure 11: Variation of the relative blowing times versus the observed pulse frequencies for the GPC individuals. Frequencies $f_{Pulse} \geq 100$ Hz have to be treated with care due to sampling issues.

Figure 11 shows the relative blowing time versus pulse frequency f_{Pulse} for all the GPC individuals. Except for individuals 2 and 5, the majority of the control laws show a major contribution of frequencies greater than 130 Hz.

Particularly, a major contribution of frequencies $f_{Pulse} \geq 250$ Hz are observed for individual 6 which explains the origin of the low AVG blowing velocity due to the limited switching speed of the valves. This leads to a significant amount of time for which the valves are only partially opened.

For individual 2, the major frequency contribution is observed at $f_{\text{Pulse}} \approx 24 \text{ Hz}$ while individual 5 presents a major frequency actuation in the range of $f_{\text{Pulse}} = 55 - 110 \text{ Hz}$. Those two individuals present a particular interest as previous experiments have shown that the Kelvin-Helmholtz instability is present close to separation point at a frequency of $f_{\text{KH}} = 110 \text{ Hz}$ and a vortex shedding at a frequency of about $f_{\text{vs}} = 27 \text{ Hz}$. Nevertheless, the low relative c_μ induced during the individual 2 control process suggests that large periods without actuation occur, corroborated by the bad cost function value of J_{PStat} .

4.2.2 Separation length – back flow area

In this section the GPC actuation laws previously obtained are analysed in detail to understand the mechanisms behind the best performing actuation laws.

The back flow area can be defined as the area in which more than 50% of the samples have a negative velocity. The resulting region is used to obtain the position of the attachment and thus the separation length L_{Sep} (Tab. 4) and the size of the back flow area.

Table 4: Separation length and percentage of reduction with respect to the baseline for the best open-loop and the GPC individuals.

	L_{Sep}/h	Reduction (%)
Baseline	5.4	-
Best open-loop	3.14	41.9
Indiv. 1	3.31	38.7
Indiv. 2	4.05	25.0
Indiv. 3	3.43	36.5
Indiv. 4	3.50	35.2
Indiv. 5	3.12	42.2
Indiv. 6	3.46	35.9
Indiv. 7	3.16	41.5
Indiv. 8	3.47	35.7

When the best open-loop control is applied, the attachment point moves upstream and the separation length decreases by 41.9% compared to the baseline case. For closed-loop control, L_{Sep} decreases by

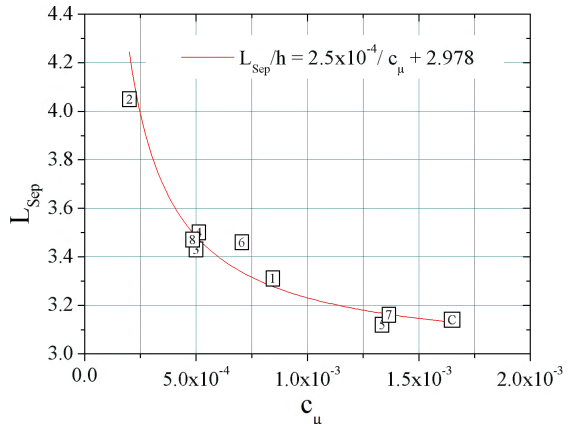


Figure 12: Variation of the separation length versus the momentum coefficient for the best open-loop (label c) and the GPC individuals.

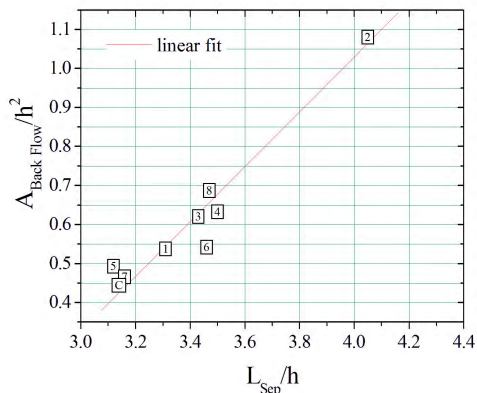


Figure 13: Variation of the mean back flow area versus the separation length for the best open-loop (label c) and the GPC individuals.

25–42% depending on the individual. Particularly, individuals 5 and 7 achieve almost the same separation length reduction (42 and 41.5%, respectively, see Tab. 4) as the best open-loop solution while having a lower c_μ consumption. Except for individual 6, the position of the mean attachment point L_{Sep}/h against c_μ (Fig. 12) presents an hyperbolic behaviour even though the actuation laws and thus mechanisms

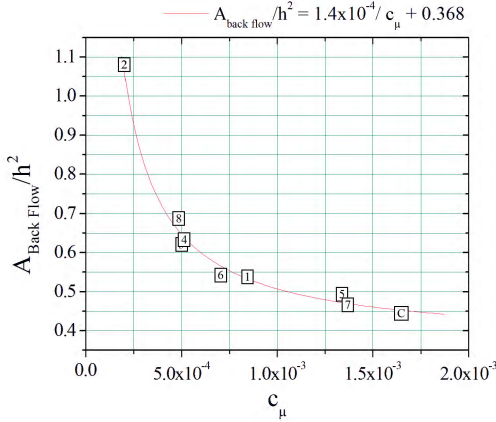


Figure 14: Variation of the mean back flow area versus the momentum coefficient for the best open-loop (label c) and the GPC individuals.

differ from each other.

In the same way, the back flow area is determined. Its evolution versus the separation length (Fig. 13) presents a linear behaviour, except for individuals 5 and 6. This result shows that the observation of the back flow area is equivalent to the observation of the variation of the separation length. This is in agreement with the recent work of Gautier and Aider (2013). Furthermore, the monotonic evolution of the back flow area versus the momentum coefficient (Fig. 14) shows that in the given setup, the momentum coefficient seems to have the greatest impact on the reduction of the separation length.

4.2.3 Kinetic and turbulent kinetic energy flow rate

In this section, we discuss the GPC individuals in terms of their energy content. For that purpose, we introduce the mean kinetic energy flow rate (M_{E_c}) and the turbulent kinetic energy flow rate (M_k) respectively defined as:

$$M_{E_c} = \int_S (\vec{U}(x) \cdot \vec{n}) E_c(x) dS(x), \quad \text{and} \quad (12)$$

$$M_k = \int_S (\vec{U}(x) \cdot \vec{n}) k(x) dS(x). \quad (13)$$

where \vec{U} is the mean velocity and \vec{n} denotes the outward-pointing normal to S . E_c represents the energy transported by the mean velocity and k is the turbulent kinetic energy (TKE). Since the turbulent production term is expected to be damped when the recirculation region is reduced, the energy transported by the mean velocity downstream of the reattachment point is expected to be larger when control occurs. If one applies flow control, M_k is governed by two properties: the modification of TKE value in the wake and the thickness of the wake. Thus, a control with a small c_μ should increase the TKE by increasing the mixing without reducing the wake thickness. As c_μ increases further, the thickness of the wake should decrease, leading to a decrease of M_k .

Figures 15 and 16 show M_{E_c} and M_k (at $x/h = 5.5$) versus c_μ and respectively versus the size of back flow area. M_{E_c} versus c_μ does not exhibit a clear trend (Fig. 15). First a large increase is observed for $c_\mu \leq 8.45 \times 10^{-4}$. For $c_\mu > 8.45 \times 10^{-4}$ the data levels out in a plateau with 3% fluctuations in M_{E_c} . In contrast, M_{E_c} decreases linearly against the back flow area as seen in Fig. 16. Furthermore, for similar back flow area value, this curve highlights more efficient individuals with a large M_{E_c} , for example individual 7 compared to the best open-loop control

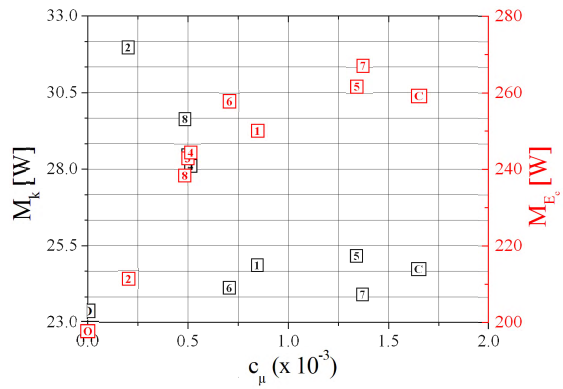


Figure 15: Variation of the turbulent kinetic energy flow rate M_k and mean kinetic energy flow rate M_{E_c} versus the momentum coefficient at $x/h = 5.5$ for the baseline (label o), for the best open-loop (label c) and for the GPC individuals.

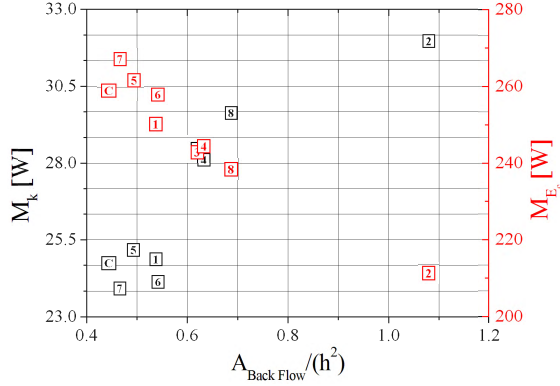


Figure 16: Variation of the turbulent kinetic energy flow rate M_k and mean kinetic energy flow rate M_{E_c} versus the mean back flow area at $x/h = 5.5$ for the best open-loop (label c) and for the GPC individuals.

or individual 6 compared to individual 1.

This efficiency variation could be related to two parameters: the shaping of the wake caused by the form of a particular control law or the overall mass flow value c_μ used by the control law. For individual 7 and the best open-loop, the control process could suggest that the physical process involved to control the flow could be responsible for M_{E_c} 's efficiency variation. Nevertheless, Fig. 11 shows that frequencies injected in the flow for individuals 1 and 6 present a similar broad bandwidth but c_μ is decreased by 17% for individual 6. As mentioned earlier, this large reduction of c_μ is due to low V_{Jet} induced by the time response of the valves. For this case, a 17% c_μ reduction is responsible for a 3% M_{E_c} increase.

The evolution of M_k versus c_μ is related to M_{E_c} : for $c_\mu \leq 8.45 \times 10^{-4}$, M_k decreases quickly with growing c_μ and for $c_\mu > 8.45 \times 10^{-4}$ it levels off in a plateau-like shape with 5% fluctuations. The evolution of M_k versus the back flow area present a global trend where M_k increases with the back flow area, as expected. Furthermore, the evolution of M_{E_c} and M_k versus c_μ indicates the existence of a plateau beginning at a c_μ value greater than the c_μ value of individual 6 (7.10^{-4}), confirming its efficiency regarding those parameters.

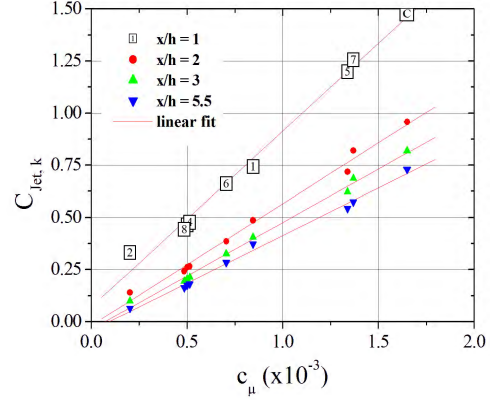


Figure 17: Variation of the coefficient $C_{\text{Jet},k}$ versus the momentum coefficient at four streamwise locations for the best open-loop (label c) and for the GPC individuals.

Analogous to M_{Jet} , a criterium M_k given by (13) is introduced using the TKE flow rate, which allows to obtain a coefficient $C_{\text{Jet},k}$ given by:

$$C_{\text{Jet},k} = \frac{M_{\text{Jet}}}{M_k}. \quad (14)$$

This coefficient $C_{\text{Jet},k}$ is plotted versus c_μ in Fig. 17. It appears that the relation between $C_{\text{Jet},k}$ and c_μ is linear. To explain this relation, we can first refer to the relation of M_{Jet} and M_k versus c_μ . Considering a quasi constant V_{Jet} blowing, $M_{\text{Jet}} \propto c_\mu$ while $M_k \propto c_\mu^{-1}$ for $c_\mu \leq 8.45 \times 10^{-4}$ and $M_k \propto c_\mu^0$ for $c_\mu \geq 8.45 \times 10^{-4}$. Furthermore, comparing the relative variation ΔM_{Jet} ($\sim \frac{M_{\text{JetMax}} - M_{\text{JetMin}}}{M_{\text{Jet}}}$) and ΔM_k , it appears that $\Delta M_{\text{Jet}} \approx 10 \Delta M_k$. So $C_{\text{Jet},k}$ is governed by M_{Jet} which presents a linear relation with c_μ .

The study of the different individuals shows that GPC is able to provide three individuals which achieved the best performance with respect to their respective cost-function. Also, it shows that accordingly to the goal to be achieved GPC explores the different mechanisms that can be used to optimize the cost function. If one looks at the separation properties, individuals 5 and 7 appear to be the most effi-

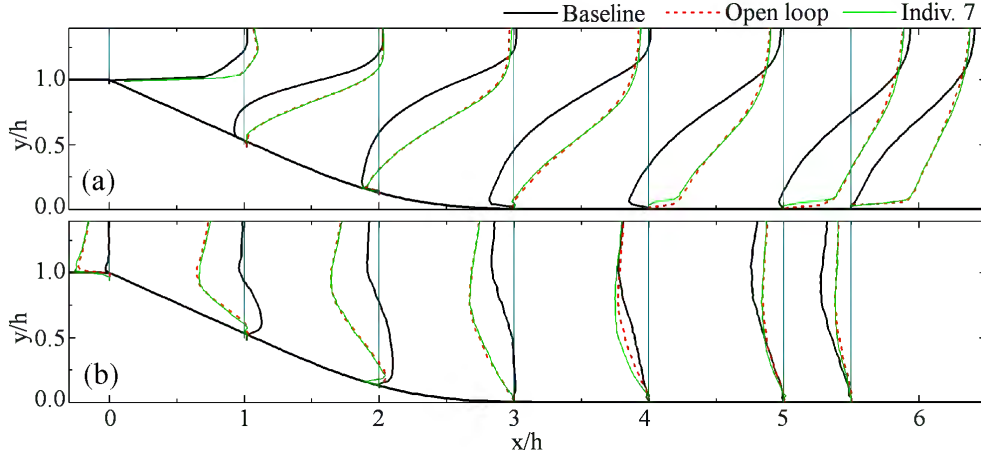


Figure 18: Mean streamwise velocity $x/h + U/U_\infty$ (a) and wall-normal velocity $x/h + 2.5 \times V/U_\infty$ (b) over the sharp edge ramp for the baseline, best open-loop and GPC individual 7.

cient individuals whereas if one looks at the energy flow rate, individual 6 showed the best performance. It shows a reduction in c_μ of 46% compared to open-loop whereas individuals 5 and 7 have a similar c_μ to open-loop. Consequently, the separation length of individual 6 is larger than the open-loop case.

4.3 Analysis of the individual 7

As observed above, the individual 7 can be ranked among the most efficient solutions and presents a similar c_μ value to the best open-loop control. For these reasons, an in-depth flow analysis of the individual 7 is now performed by comparison to the best open-loop control.

The expression for this individual is given below:

$$b(t) = -1.23 \frac{0.59 + s_1 + s_2 + \tanh(s_2)}{s_2 s_5} + \ln \left(\frac{s_5 + s_3}{s_4 + s_5} \right) \quad (15)$$

The division and the natural logarithm are capped so that there exist no division by 0 as explained in Sec. 3.

As shown in Fig. 18(a), AVGs promote the momentum transfer between the near wall and the free stream yielding a larger mean streamwise velocity in

the neighborhood of the sharp edge. In addition, the counter-rotating vortices generated by the AVGs induce a significant sweep flow motion at the laser sheet position. This is evidenced by the strong negative mean transverse velocity close to the sharp edge. Combined together, these mechanisms delay the separation and deflect the separated shear layer towards the wall yielding a shorter recirculation (see Fig. 19).

For the baseline case, a higher level of TKE (see Fig. 19 (a)) is observed close to the center line of the shear layer which is progressively deflected towards the wall. At the attachment point, the angle of deflection of shear layer corresponds to 3.3° . The maximum TKE value $k/U_\infty^2 \approx 0.56$ is achieved close to the separation point. It decreases quickly down to a minimal value of $k/U_\infty^2 \approx 0.24$ in the shear layer at $x/h \approx 0.63$. Beyond this point, the TKE increases in the shear layer up to the reattachment point ($k/U_\infty^2 \approx 0.5$). On the other hand, the recirculation bubble below the shear layer is characterized by a low level of TKE ($5 \times 10^{-3} \leq k/U_\infty^2 \leq 1 \times 10^{-2}$).

For the best open-loop, the evolution of the TKE in the shear layer is similar to the baseline case but higher levels are observed downstream from the separation point ($k/U_\infty^2 \approx 0.75$). This maximal value decreases up to $x/h = 1$ ($k/U_\infty^2 \approx 0.54$) and then

increases progressively up to the attachment point ($k/U_\infty^2 \approx 0.58$). At the attachment point, the shear layer center line shows a larger angle of deflection of 9.6° . This intensification of the TKE shows also in the recirculation bubble where $0.3 \leq k/U_\infty^2 \leq 0.5$. As already observed in Debien et al (2015), this intensification in the TKE is due to the lock-on of vortex shedding by the actuators, which is responsible for the generation of large spanwise structures along the ramp.

For the individual 7, the evolution of the TKE in the shear layer presents an important difference since a progressive increase from separation point ($k/U_\infty^2 \approx 0.5$) up to reattachment point ($k/U_\infty^2 \approx 0.54$) occurs. At the reattachment point, the shear layer center line shows also a large angle of deflection of 9° . The recirculation bubble presents also an intensification in the TKE level but a thin layer with low TKE level ($0.1 \leq k/U_\infty^2 \leq 0.2$) is present above the ramp from $x/h \geq 0.55$ up to attachment point. It appears that contrary to the best open-loop control where large scale structures are generated by the AVGs blowing to enhance mixing in recirculation bubble, the GPC control strategy seems to stimulate the development of shear layer and to stabilize it as it does not show maximal TKE level near separation point but a fast growth of TKE level is achieved downstream of the separation point.

The evolution of the vorticity thickness (δ_ω) of the shear layer above the separation zone is presented Fig. 20 for the baseline, the best open-loop and the GPC individual. As observed by Castro and Haque (1987) and Jovic (1996), the vorticity thickness is featured by a large growth rate which progressively decreases up to the reattachment point. Using a linear fit in the least-square sense, the growth rate of the separated shear-layer for both the baseline and the best open-loop solution cases is $\frac{\partial \delta_\omega}{\partial(x/h)} = 0.17$ over the range $0.25 \leq x/L_{\text{Sep}} \leq 0.6$. This value is close to that reported for free shear-layers (see e.g.(Browand and Troutt, 1985)). The growth rate of the separated shear-layer induced by the individual 7 seems to be larger $\frac{\partial \delta_\omega}{\partial(x/h)} = 0.25$ (see Fig. 20). Note that unlike baseline and the GPC individuals, the best open-loop control vorticity thickness grows exponentially up to

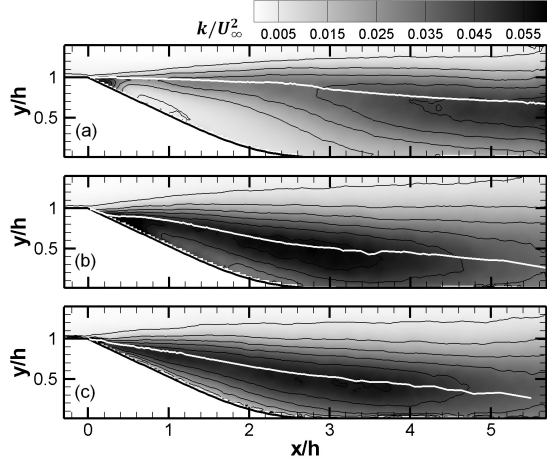


Figure 19: Turbulent kinetic energy for the baseline (a), the best open-loop (b) and the GPC individual 7 (c). White line corresponds to the center line of the shear layer.

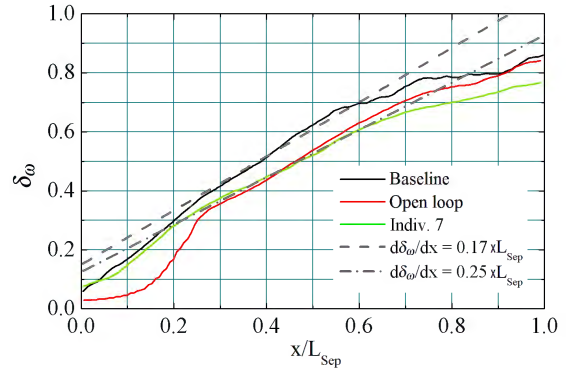


Figure 20: Streamwise variation of the vorticity thickness over the ramp for baseline, best open-loop and GPC individual 7.

$x/L_{\text{Sep}} = 0.25$ before its linear growth. This change coincides with the occurrence of high levels of TKE. For the best open-loop control, a low actuation frequency is used to lock on the shedding frequency. Streamwise vortices are supposed to be produced by the low AVGs' activation frequency, and these vortices are able to develop up to $x/L_{\text{Sep}} \approx 0.25$ despite

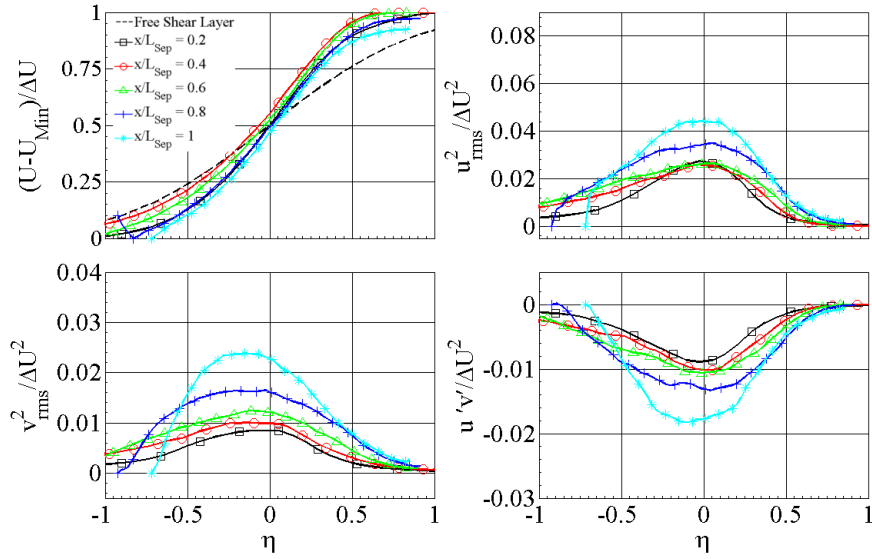


Figure 21: Mean streamwise velocity and Reynolds stresses profiles of the mixing layer in similarity coordinates for the baseline.

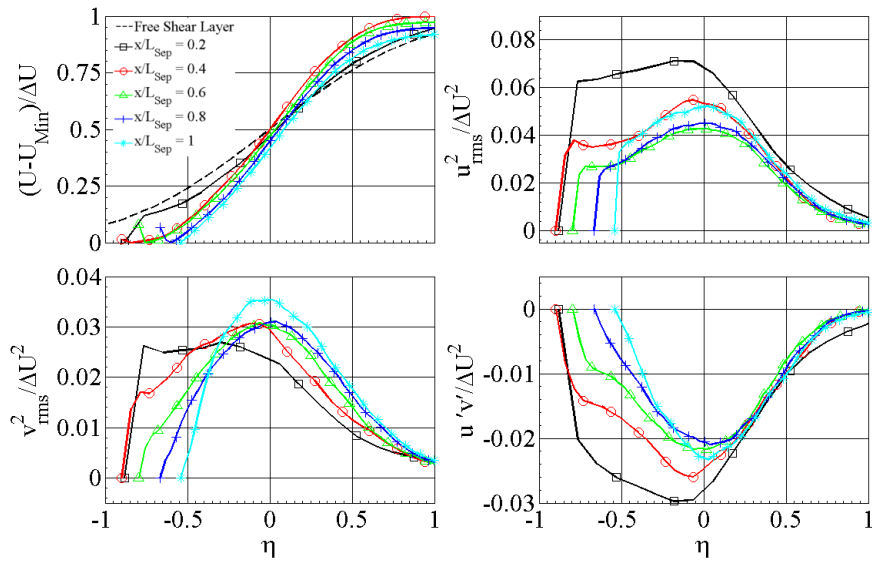


Figure 22: Mean streamwise velocity and Reynolds stresses profiles of the mixing layer in similarity coordinates for the best open-loop.

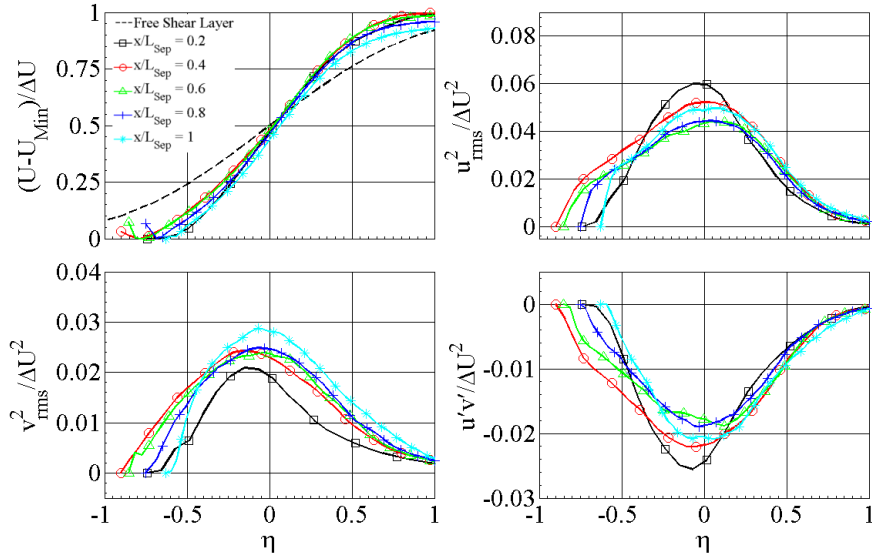


Figure 23: Mean streamwise velocity and Reynolds stresses profiles of the mixing layer in similarity coordinates for the GPC individual 7.

the presence of the sharp edge (Debien et al, 2015). Beyond $x/L_{\text{Sep}} \geq 0.25$, the classic development of the shear layer occurs.

In order to compare the shear-layers developing above the recirculation region, mean velocity profiles and Reynolds stresses are plotted in dimensionless form in Figs. 21, 22 and 23 for the baseline, the open-loop control and the closed-loop control cases, respectively. For that purpose, the reduced coordinate $\eta = \frac{y-y_c}{\delta_\omega}$ is used, where y_c corresponds to the position of maximal velocity gradient (see Fig. 19 in which the white line corresponds to y_c). The velocity difference $\Delta U = U_\infty - U_{\text{Min}}$ is used as the reference velocity, where U_{Min} is the minimum streamwise velocity of the profile. For the baseline case (Fig. 21), the dimensionless mean streamwise velocity profiles do not reach a self-similar state which seems to be induced by the presence of the separation bubble which mainly affects the evolution of the lower part of velocity profiles ($\eta \leq 0$) and of the maximal velocity gradient along the ramp. For the best open-loop (Fig. 22) and the individual 7 (Fig. 23), the dimensionless mean streamwise velocity profiles

collapse downstream from $x/L_{\text{Sep}} \geq 0.25$, achieving a nearly self-similar state.

The baseline case presents higher Reynolds stresses levels close to the shear layer center line (Castro and Haque, 1987) while low Reynolds stresses levels are observed close to the wall in the separation bubble, consistent with the literature (Song et al, 2000). From the sharp edge ramp, the high level of $u'^2_{\text{rms}}/\Delta U^2$ in the shear layer progressively decreases up to 0.024 at $x/L_{\text{Sep}} = 0.5$ and then increases up to reattachment point. In contrast, $v'^2_{\text{rms}}/\Delta U^2$ and $u'v'/\Delta U^2$ increase from separation point up to attachment point where $v'^2_{\text{rms}}/\Delta U^2 = 0.028$ and $u'v'/\Delta U^2 = -0.018$.

The actuation introduced by the AVGs increases the Reynolds stresses levels in the recirculating bubble. In the shear layer, both open-loop and indiv. 7 have similar characteristics. $u'^2_{\text{rms}}/\Delta U^2$ presents higher level close to the separation point, decreases up to $x/L_{\text{Sep}} = 0.6$ and then increases up to the attachment point. $v'^2_{\text{rms}}/\Delta U^2$ presents an increase from separation point up to attachment point. Downstream a plateau at $0.4 \leq x/L_{\text{Sep}} \leq 0.8$ for open-

loop, and $0.4 \leq x/L_{\text{Sep}} \leq 0.5$ for individual 7 is visible. The shear component $u'v'/\Delta U^2$ decreases up to $x/L_{\text{Sep}} = 0.7$ for both cases. Furthermore, the local maximum of $\frac{v_{\text{rms}}^2}{\Delta U^2}$ and $\frac{u'v'}{\Delta U^2}$ are shifted towards the lower part of the shear layer ($\eta \leq 0$) close to the separation point (see $x/L_{\text{Sep}} = 0.2$, Fig. 22 and 23). For the best open-loop control, near wall Reynolds stresses present high value for $x/L_{\text{Sep}} \leq 0.6$ due to the convection of large vortices created by the AVGs (Debien et al, 2015).

The dimensionless Reynolds stresses reveal drastic changes between the baseline and the controlled cases. The decrease of the shear Reynolds stresses component up to $x/L_{\text{Sep}} = 0.7$ when control is applied suggests that the shear layer development is stimulated by AVGs' blowing. This could explain the self-similar state of the dimensionless streamwise mean velocity achieved with flow control implying that the driving of the shear layer development is due to the convection and growth of structures induced by the AVGs' blowing.

The extraction of the vortex region Ω is now obtained using the vector field topology. The area of the detected vortex region Ω_A is extracted to obtain the vortex area distribution that is presented in Fig. 24 for the baseline case, the best open-loop control and the individual 7. Overall, 50% of the detected vortices occupy an effective area Ω_A smaller than $0.01h^2$. The cumulative distributions plotted in Fig. 24 evidence that the GPC control induce the production of smaller vortices compared to both baseline and open-loop control. This property may somehow be related to the broad range of frequencies excited by the GPC control law. For the open-loop case, we have reported elsewhere (see Debien et al (2015)) a lock-on mechanism responsible for the generation of shedded large-scale structures. Therefore, even though both control strategies mainly act on the growth of the separated shear-layer, the results displayed in Fig. 24 suggest two different mechanisms leading to a nearly identical mean separation region: i. a rapid growth of the shear-layer due to large-scale structure engulfment (open-loop) and ii. an enhancement of the local mixing of the shear-layer (GPC).

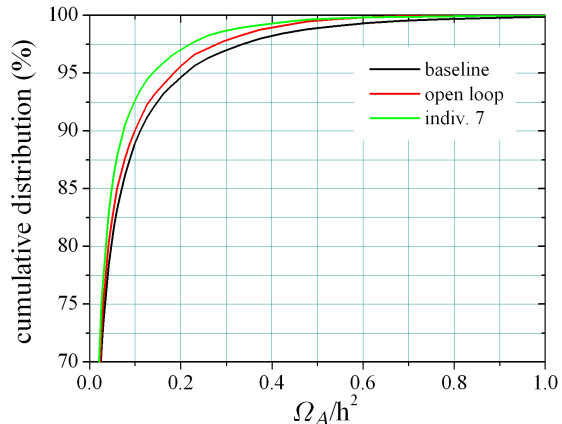


Figure 24: Cumulative distribution of area of the detected vortex regions for the baseline, the best open-loop and GPC individual 7.

5 Conclusions

Genetic programming control (GPC) has been applied to closed-loop forcing of a separated turbulent boundary layer over a sharp edge ramp using only the signal of two hot-film sensors placed near the inflection point of the ramp and static pressure sensors along the ramp. GPC achieves control laws aiming to reduce the separation length with a penalized momentum coefficient. The resulting law minimizes a given cost function. The performance is monitored by the pressure distribution, the hot-film signals and the momentum coefficient. By varying the actuation penalization of the cost function, multiple optimization points were obtained.

The performance of GPC is benchmarked with the optimized periodic actuation. The reduction of the separation length, the back flow area, and the pressure distribution is similar but GPC achieves this separation mitigation with a smaller momentum coefficient. This can be explained by the direct relation between the momentum coefficient, the separation length and the back flow area. Furthermore, the kinetic energy of the mean flow field reveals that GPC achieves a better increase in the kinetic energy than the best open-loop control.

The velocity field properties were analyzed using a Stereo PIV system. Similar performance benefits are obtained with open and closed-loop control. For the best open-loop control, the actuation frequency is chosen close to shedding mode to obtain a lock-on control. Downstream, the flow displays the streamwise vortices signature induced by the AVGs up to $x/L_{\text{Sep}} = 0.25$. Beyond this point, the classic shear layer develops and presents a similarity state for the mean streamwise velocity, induced by the growth and convection of large vortex region achieving the reduction of separation length. In contrast, the analysis of the best GPC laws show much higher actuation frequencies from twice to ten times the best open-loop frequency. The vector field analysis also reveals that streamwise vorticity signature induced by the AVGs is not observed downstream from the sharp edge ramp. Furthermore, the shear layer growth is increased as compared to the baseline case. The GPC-controlled shear layer displays a mean streamwise velocity similarity state beyond $x/L_{\text{Sep}} = 0.25$. The mean vortex region downstream of the sharp edge ramp grows monotonically for GPC-based closed-loop control — corroborating the rapid development of the shear layer. As expected for high-frequency forcing, GPC yields a finer distribution of vortex region population as compared to baseline or best open-loop control. Summarizing, GPC yields similar actuation benefits as best open-loop control but at lower momentum coefficient. This improvement is based on distinctly different high-frequency flow structures, not on the lock-on of the periodic actuation response.

acknowledgements

This work was supported by French National Research Agency (ANR) via the SepaCoDe Project (ANR-11-BS09-018) and the TUCOROM Chair of Excellence (ANR-10-CEXC-0015).

References

- Amitay M, Glezer A (2002) Role of actuation frequency in controlled flow reattachment over a stalled airfoil. *AIAA J* 40(2):209–216
- Benard N, Moreau E, Griffin J, Cattafesta III LN (2010) Slope seeking for autonomous lift improvement by plasma surface discharge. *Exp Fluids* 48(5):791–808
- Benedict LH, Gould RD (1996) Towards better uncertainty estimates for turbulence statistics. *Exp Fluids* 22(2):129–136
- Browand FK, Troutt TR (1985) The turbulent mixing layer: geometry of large vortices. *J Fluid Mech* 158:489–509
- Brunton SL, Noack BR (2015) Closed-loop turbulence control: Progress and challenges. *Appl Mech Rev* (in print)
- Castro IP, Haque A (1987) The structure of a turbulent shear layer bounding a separation region. *J Fluid Mech* 179:439–468
- Cherry NJ, Hillier R, Latour MEMP (1984) Unsteady measurements in a separated and reattaching flow. *J Fluid Mech* 144:13–46
- Cordier L, Noack BR, Tissot G, Lehnasch G, Delville J, Balajewicz M, Daviller G, Niven RK (2013) Identification strategy for model-based control. *Exp in Fluids* 54:1580
- Cuvier C, Braud C, Foucault JM, Stanislas M (2011) Flow control over a ramp using active vortex generators. In: *Seventh International Symposium on Turbulence and Shear Flow Phenomena*, Ottawa, Canada
- Dandois J, Garnier E, Sagaut P (2007) Numerical simulation of active separation control by a synthetic jet. *J Fluid Mech* 574(1):25–58
- Debien A, Aubrun S, Mazellier N, Kourta A (2014) Salient and smooth edge ramps inducing turbulent boundary layer separation: Flow characterization for control perspective. *C R Mécanique*

- Debien A, Aubrun S, Mazellier N, Kourta A (2015) Active separation control process over a sharp edge ramp. In: Ninth International Symposium on Turbulence and Shear Flow Phenomena, Melbourne, Australia
- Duriez T, Parezanović V, Laurentie JC, Fourment C, Delville J, Bonnet JP, Cordier L, Noack BR, Segond M, Abel MW, Gautier N, Aider JL, Raibaud C, Cuvier C, Stanislas M, Brunton S (2014) Closed-loop control of experimental shear layers using machine learning (Invited). In: 7th AIAA Flow Control Conference, Atlanta, Georgia, USA, pp 1–16
- Gautier N, Aider JL (2013) Control of the separated flow downstream of a backward-facing step using visual feedback. *Proc R Soc A* 469(2160):20130,404
- Gautier N, Aider JL, Duriez T, Noack BR, Segond M, Abel M (2015) Closed-loop separation control using machine learning. *J Fluid Mech* 770:442–457
- Gerhard J, Pastoor M, King R, Noack BR, Dillmann A, Morzyński M, Tadmor G (2003) Model-based control of vortex shedding using low-dimensional Galerkin models. In: 33rd AIAA Fluids Conference and Exhibit, Orlando, Florida, USA, paper 2003-4262
- Godard G, Stanislas M (2006a) Control of a decelerating boundary layer. Part 1: Optimization of passive vortex generators. *Aerosp Sci Technol* 10(3):181–191
- Godard G, Stanislas M (2006b) Control of a decelerating boundary layer. Part 3: Optimization of round jets vortex generators. *Aerosp Sci Technol* 10(6):455–464
- Greenblatt D, Wygnanski IJ (2000) The control of flow separation by periodic excitation. *Prog Aerosp Sci* 36(7):487–545
- Hasan MAZ (1992) The flow over a backward-facing step under controlled perturbation: laminar separation. *J Fluid Mech* 238:73–96
- Jovic S (1996) An experimental study of a separated/reattached flow behind a backward-facing step. $Re_H = 37,000$. Tech. Mem. 110384, NASA
- King R (ed) (2007) Active Flow Control I, no. 95 in Notes on Numerical Fluid Mechanics and Interdisciplinary Design, Springer-Verlag, Berlin
- King R (ed) (2010) Active Flow Control II, no. 108 in Notes on Numerical Fluid Mechanics and Interdisciplinary Design, Springer-Verlag, Berlin
- Koza JR (1992) Genetic Programming: On the Programming of Computers by Means of Natural Selection. The MIT Press, Boston
- Koza JR, Bennett III FH, Stiffelman O (1999) Genetic Programming as a Darwinian Invention Machine, Lecture Notes in Computer Science, vol 1598. Springer
- Lin JC (2002) Review of research on low-profile vortex generators to control boundary-layer separation. *Prog Aerosp Sci* 38(4):389–420
- Mabey DG (1972) Analysis and correlation of data on pressure fluctuations in separated flow. *J Aircraft* 9(9):642–645
- Mittal R, Kotapati R, Cattafesta III L (2005) Numerical Study of Resonant Interactions and Flow Control in a Canonical Separated Flow. In: AIAA 43rd Aerospace Sciences Meeting and Exhibit, Reno, NV, USA
- Murphy KP (2012) Machine Learning: A Probabilistic Perspective. MIT Press, Cambridge
- Parezanovic V, Laurentie JC, Fourment C, Delville J, Bonnet JP, Spohn A, Duriez T, Cordier L, Noack BR, Abel M, Segond M, Shaqarin T, Brunton S (2015) Mixing layer manipulation experiment – from open-loop forcing to closed-loop machine learning control. *Flow Turbul Combust* 94:155–173
- Pastoor M, Henning L, Noack BR, King R, Tadmor G (2008) Feedback shear layer control for bluff body drag reduction. *J Fluid Mech* 608:161–196

- Petz C, Kasten J, Prohaska S, Hege HC (2009) Hierarchical Vortex Regions in Swirling Flow. *Comput Graph Forum* 28(3):863–870
- Rowley CW, Williams DR (2006) Dynamics and control of high-Reynolds number flows over open cavities. *Annu Rev Fluid Mech* 38:251–276
- Seifert A, Pack LG (2003) Effects of sweep on active separation control at high Reynolds numbers. *J Aircraft* 40(1):120–126
- Shaqarin T, Braud C, Coudert S, Stanislas M (2011) Open and closed-loop experiments to reattach a thick turbulent boundary layer. In: *Seventh International Symposium on Turbulence and Shear Flow Phenomena, Ottawa, Canada*
- Shaqarin T, Braud C, Coudert S, Stanislas M (2013) Open and closed-loop experiments to identify the separated flow dynamics of a thick turbulent boundary layer. *Exp Fluids* 54(2):1–22
- Song S, DeGraaff DB, Eaton JK (2000) Experimental study of a separating, reattaching, and redeveloping flow over a smoothly contoured ramp. *Int J Heat Fluid Fl* 21(5):512–519
- Tennekes H, Lumley J (1972) *A first course in Turbulence*. MIT Press
- Zaman KBMQ, Hussain AKMF (1981) Turbulence suppression in free shear flows by controlled excitation. *J Fluid Mech* 103:133–159